Predicting the Excitation Dynamics in Lanthanide Nanoparticles

Simon Spelthann,* Jonas Thiem, Oliver Melchert, Rajesh Komban, Christoph Gimmler, Ayhan Demicran, Axel Ruehl, and Detlev Ristau

With their dipole-forbidden 4f transitions, lanthanides doped in nanoparticles promise high excited state lifetimes and quantum yields that are required for applications such as composite lasers or nanoscale quantum memories. Quenching at the nanoparticle surface, however, severely reduces the lifetime and quantum yield and requires resource-consuming experimental optimization that could not be replaced by simulations due to the limitations of existing approaches until now. Here, a versatile approach is presented that fully accounts for spatiotemporal dynamics and reliably predicts the lifetimes and quantum yields of lanthanide nanoparticles. $LiYF_4:Pr^{3+}$ nanoparticles are synthesized as a model system, and the lifetimes of a concentration series ($\approx$10 nm, 0.7–1.47 at%) are used to match the model parameters to the experimental conditions. Employing these parameters, the lifetimes and quantum yields of a size series ($\approx$5 at%, 12–21 nm) are predicted with a maximum uncertainty of 12.6%. To demonstrate the potential of the model, a neutral shell is added around the core particles in the model which extends the lifetime by up to 44%. Furthermore, spatiotemporal analysis of single nanoparticles points toward a new type of energy trapping in lanthanide nanoparticles. Consequently, the numerical optimization brings applications such as efficient nanoparticle lasers or quantum memories within reach.

S. Spelthann, J. Thiem, O. Melchert, A. Demicran, A. Ruehl, D. Ristau
Leibniz University Hannover
Institute of Quantum Optics
Welfengarten 1, D-30167 Hannover, Germany
E-mail: spelthann@iqo.uni-hannover.de

O. Melchert, A. Demicran, D. Ristau
Cluster of Excellence PhoenixD
Welfengarten 1A, D-30167 Hannover, Germany

R. Komban, C. Gimmler
Fraunhofer Center for Applied Nanotechnology CAN
Grindelallee 117, D-20146 Hamburg, Germany

A. Ruehl, D. Ristau
QUEST Leibniz Research School
Callinstraße 36, D-30167 Hannover, Germany

1. Introduction

Trivalent lanthanide ions doped in a crystalline environment provide magnificent optical storage capacities, that is, excited state lifetime in the μs to ms range, since the optical transitions are forbidden by electric dipole interaction thus making these materials excellent candidates for lasers, phosphors, or quantum memories.[1–3]

In nanoparticles, lanthanide ions inspired a broad range of new applications such as nanothermometry or nanobiomedicine.[4–7] At the nanoscale, however, quenching mechanisms at the particle surface severely reduce both the excited state lifetime and quantum yield thus limiting the nanoparticles' field of application. Consequently, researchers make enormous efforts to optimize the excited state lifetime and quantum yield of lanthanide nanoparticles.[8,9]

To gain deeper insights in the underlying dynamics, researchers started to complement their experimental investigations with numerical simulations. Most prominently, this has been the case for upconverting nanoparticles that allow for nonlinear excitation of anti-Stokes emission by co-doping,[10–15] modeled in terms of a set of differential rate equations. This approach is widely used to model lasers[1,16] and comparable approaches recently have been used to model photon avalanche emission.[17] In these rate-equation-based models, the number of energy levels taken into account determines the number of coupled equations. Every single energy level of the involved lanthanide ions is assigned an individual differential equation that includes all relevant population and de-population processes. Although simulations based on this approach comprise a certain optimization potential they reach their limit at some ten nanometers particle size.

The first model was developed for micron-sized particles,[18,19] a scale where the optical properties are determined by the dynamics in the volume of the particles as in bulk crystals. Rate-equation models average the properties and ionic distances of all the nanoparticles and determine the transition rates in terms of a single macroscopic variable. Consequently, the model considers only one process rate for the average distances, that is, for example one rate for energy transfer in the whole nanoparticle.[20]

**ADVANCED
SCIENCE NEWS**

www.advancedsciencenews.com

**ADVANCED
OPTICAL
MATERIALS**

www.advopticalmat.de

However, to accurately model nanoscopic particles, spatial dynamics have to be considered because surface effects become increasingly important at this scale.[21–23] Subsequently, researchers continued to develop rate-equation-based approaches toward enabling spatial resolution of the excitation dynamics. In 2015, Villanueva–Delgado and co-workers presented an approach that takes the inter-ionic distances into account and averages the rates of every ion within a nanoparticle, instead of calculating the rate of an average distance.[23–25] Pini and co-workers recently extended this model by dividing the nanoparticles into a core and an outer layer that interacts with the surrounding medium and achieved a certain spatial resolution in 40 nm sized nanoparticles.[26]

To summarize, rate equations can describe macroscopic and, to some extent, microscopic systems particularly well as long as surface effects can be neglected.[1,16–19,23–27] Therefore, all these rate equation-based models provided an increasingly accurate understanding of the underlying dynamics within lanthanide nanoparticles.

However, these simulations reach their limits at nanoscopic scales, which restricts them to a complementary role in nanoparticle research. Consequently, existing numerical approaches cannot exploit the potential for understanding and predicting spatial excitation dynamics in lanthanide nanoparticles. This prevents high lifetimes and simultaneously high quantum yields in these particles.

Here, we present a numerical model based on a Monte Carlo approach that allows us to understand, and, more importantly, to predict the spatiotemporal excitation dynamics of lanthanide nanoparticles. Our model treats every lanthanide ion in a nanoparticle indiviually including all relevant processes such as energy transfers, cross-relaxations, and multiphonon quenching to the surrounding medium. We choose $LiYF_4$:Pr^{3+} as the model system since it is a downconversion material and thus less complex than upconversion or photo avalanche nanoparticles. Our modeling approach is, however, not restricted to the chosen model system but applicable to any kind of lanthanide nanoparticle system. To match the model parameters to the experimental conditions, we use a concentration series ($\approx$10 nm and 0.7 – 1.47 at%) to determine the relevant characteristic lengths of the relevant processes. With these parameters, we predict a size series' ($\approx$5 at% and 12–21 nm) excited state lifetime and quantum yield with a maximum uncertainty of 12.6%. To demonstrate the flexibility of our numerical approach we apply a prominent strategy from the literature to suppress quenching and extended the model by adding a neutral shell around the nanoparticles. This simple optimization yields an improvement of +44 % and +3.5 percentage points for the excited state lifetime and quantum yield, respectively. To highlight the central strength of our approach, the spatial resolution of the excitation dynamics, we simulate individual nanoparticles and analyze the dynamics of the mean spatial position of the excitation energy. We find that in some nanoparticles the excitation energy oscillates for a short period and infer that this points toward a new type of energy trapping in lanthanide nanoparticles. Together with the ability to predict the excited state lifetime and quantum yield, this renders our Monte Carlo approach a powerful tool for nanoparticle research that is not limited with respect to the particle size. Our model will

contribute to a deeper understanding of the dynamics in nanoparticles and, in particular, reveal new spatiotemporal effects, such as energy trapping. In addition, it will enable the numerical optimization of nanoparticles for excellent spectroscopic properties and thus open up new fields of application, such as highly efficient nanoparticle lasers or quantum memories.

2. Results and Discussion

2.1. Sample Preparation, Structural and Spectroscopic Properties

To allow for a benchmark of our numerical results with experimental values we synthesized a concentration series and a size series of $LiYF_4$:Pr^{3+} nanoparticles in a simple one-pot synthesis. In this synthesis, we heat rare earth chlorides in the presence of oleic acid which results in the in-situ forming of oleates (refer to Experimental Section for details). To obtain high-quality $LiYF_4$:Pr^{3+} nanoparticles, we needed to carefully select the optimum amount of oleic acid in combination with the right heating temperature and duration.[22]

We confirmed the purity, size, morphology, and doping concentration of the nanoparticles by X-ray diffraction (XRD), transmission electron microscopy (TEM), and energy-dispersive X-ray spectroscopy (TEM-EDX), see the Experimental Section and Figures S1–S10 (Supporting Information) for details.

The synthesis yielded high-quality monodisperse particles with a bipyramidal shape.[22,28] The concentration series consists of 4 samples with a comparable size distribution at around 10 nm. The doping concentration of these samples increases from 0.7 to 1.47 at%. Furthermore, the size series consists of five samples with comparable doping concentrations of approximately 5 at%. The size of these samples increases from around 12 to 21 nm. An overview of all samples used in this work is compiled in **Figure 1** and the respective resulting material parameters were used as input parameters to the simulations.

To fully access the experimental control parameter we measured the excited state lifetimes of the $^3P_0$ and $^1D_2$ levels as well as the quantum yield (photons emitted per photons absorbed), see the experimental section for details on the experimental procedures. We found that the lifetime is sufficient as a control parameter. We also included the quantum yield as an important indicator of the nanoparticles' performance. The $^3P_0$ lifetime for the concentration series ranges at about 50% of the bulk lifetime for $LiYF_4$ crystals with 0.65 at% Pr^{3+} content as evident from **Figure 2**a. Bulk crystals with this doping concentration are regularly used in laser physics and exhibit lifetimes of 35.7 µs.[29] Furthermore, the $^1D_2$ lifetimes of the concentration series match the lifetime of respectively doped bulk crystals and stay at a plateau of about (25 ± 2) µs for the size series, see Figure 2b. We observe a difference in the evolution of the excited state lifetimes for the $^3P_0$ and $^1D_2$ levels. In previous work, we found that the $^1D_2$ level is populated via multiphonon quenching from the $^3P_0$ level. Furthermore, the excited state lifetime of the $^1D_2$ level decreases exponentially with the number of ions within the nanoparticles and it is limited by cross-relaxation.[22] In nanoparticles of 10-20 nm size, multiphonon-quenching is thus an irrelevant process for the $^1D_2$ level while it is a relevant process for the $^3P_0$ level which results in different lifetimes. Despite the comparatively long
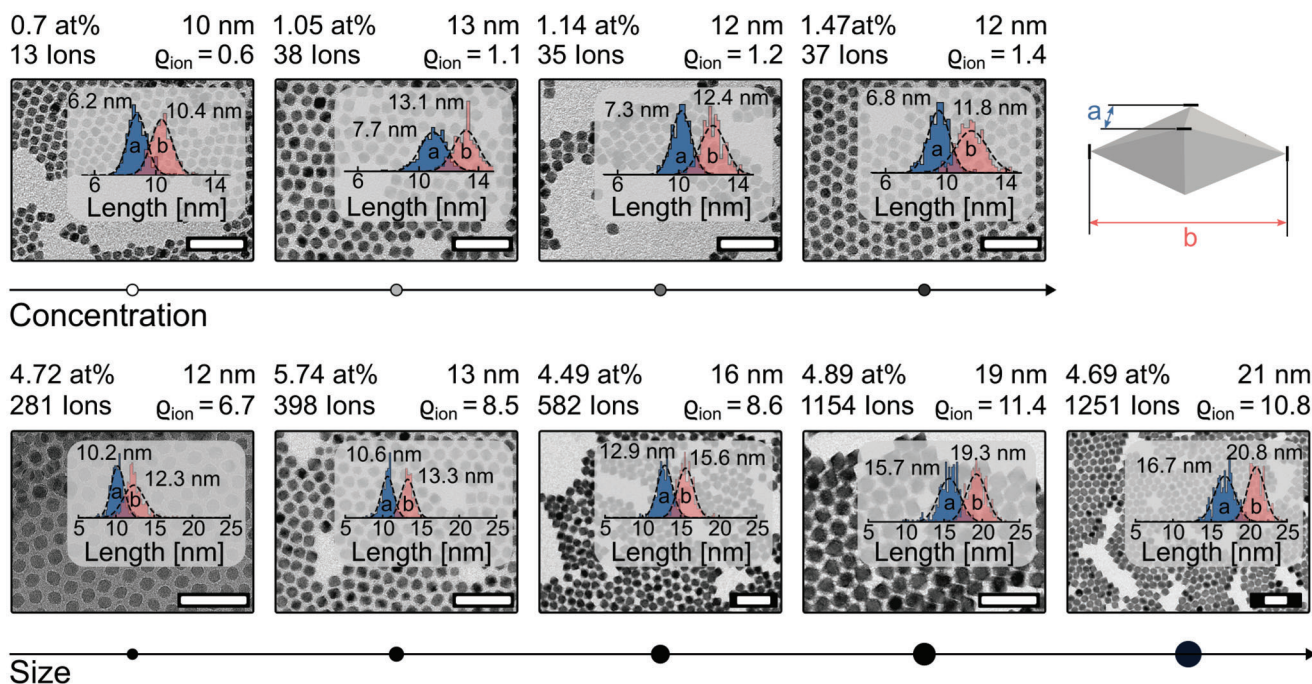
Figure 1. Overview of the samples and the data extracted from the structural material analysis. The sample set consists of a concentration series (top) and a size series (bottom). The concentration series comprises four samples with a size of approximately 10 nm and a Pr^{3+} doping concentration increasing from 0.7 to 1.47 at%. The doping concentration set includes five samples with a doping concentration of approximately 5 at% and sizes increasing from 12 to 21 nm. The ion density ρ_{Ion} is given in nm^{-3}. The scale bar in the TEM pictures corresponds to a length of 50 nm. Every sample was assigned an individual symbol (the circles of different color or size under the TEM pictures) that represents that sample in the plots throughout this work.
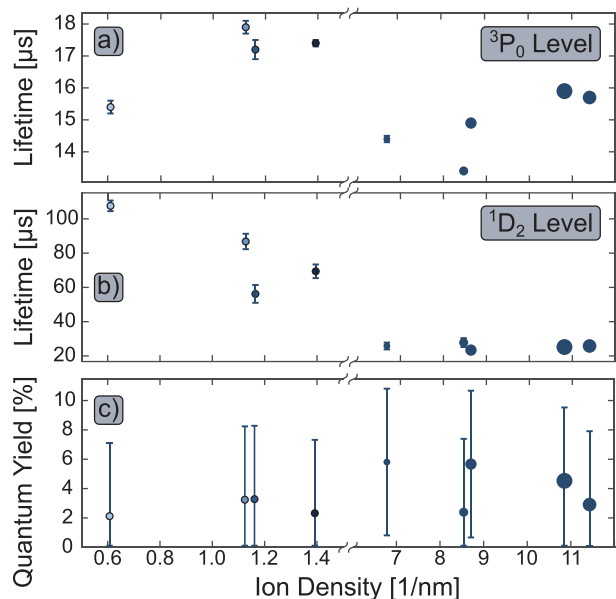

Figure 2. The experimental control parameter consists of these spectroscopic results: the excited state lifetime of a) the upper energy level $^3P_0$ and b) the subjacent $^1D_2$ level (compare Figure 3) as well as c) the quantum yield. Note that the lifetime errors are not visible for the size series since they are very small.

lifetimes, the quantum yield only exhibits a maximum of 5% with a measurement error of 5 percentage points, compare Figure 2c. We discussed the underlying mechanisms in our previous work and refer the interested reader to this publication.[22]

Since $LiYF_4:Pr^{3+}$ bulk crystals find application as laser gain medium for visible emitting lasers their optical properties are well-studied.[29–35] Numerous visible emission lines in the range from 480 to 720 nm are available through direct excitation of the $^3P_0$ level with blue light at 480 nm, see **Figure 3**a.[35] The emission of photons occurs spontaneously and can be described by the Einstein coefficient A which is the inverse of the excited state lifetime τ of a single ion in the nanocrystalline matrix. Spontaneous emission can be expressed as rate R_{SpEm} by

$$R_{SpEm} = -A \cdot t \tag{1}$$

which depends on the time t. Following, local field effects have to be taken into account since the surrounding medium affects the lifetime.[36–38]

Lanthanide ions exchange energy either via electron exchange or through dipole-dipole interaction. These processes were described by Dexter and Föster,[39,40] respectively, and take place on different length scales. While electron exchange occurs in the sub-nanometer range (typ. <20 Å) the dipole-dipole interaction can cover some nanometers (typ. <10 nm). As a result, Dexter energy transfer (DET) is referred to as energy migration and Förster energy transfer (FET) as energy hopping.[41,42]
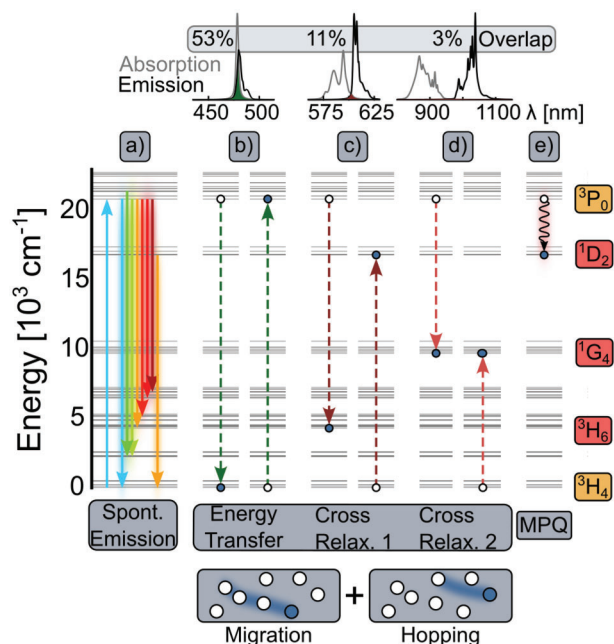
ADVANCED
SCIENCE NEWS
www.advancedsciencenews.com

ADVANCED
OPTICAL
MATERIALS
www.advopticalmat.de

Figure 3. Energy level scheme of LiYF$_4$:Pr^{3+} and graphical representation of relevant energy transfers. a) Relevant absorption and emission transitions in the visible spectrum. b–d) Energy transfer and cross relaxations. The spectral overlap between the interacting ions is shown for each energy transfer. This overlap significantly determines the characteristic length for the respective processes. Depending on the underlying physics, every process can occur as energy migration (electron exchange) or as well as energy hopping (dipole-dipole interaction). e) Multiphonon-quenching depopulates the $^3P_0$ energy level through dipole-dipole interaction with the solvent that surrounds the nanoparticles.

The rate of the Dexter energy transfer

$$R_{DET} = \frac{1}{\tau} \exp\left(\gamma \cdot \left(1 - \frac{r}{r_0}\right)\right) \qquad (2)$$

with $\gamma = 2r_0/L$ and L being the effective Bohr radius and the rate of the Förster energy transfer

$$R_{FET} = \frac{1}{\tau} \cdot \frac{d_0^6}{d^6} \qquad (3)$$

with the distances r (Dexter) and d (Förster) between donor and acceptor. Both processes depend on the excited state lifetime and a characteristic length of r_0 (Dexter) or d_0 (Förster).[39,40,43] These two lengths are defined as follows: For the so-called Dexter radius, the energy transfer rate is equal to the rate for spontaneous emission. For the Förster distance, the energy transfer rate is 50% of the rate for spontaneous emission. Both characteristic lengths depend on the energy donor's and acceptor's spectral overlap. The spectra relevant to this work are depicted in Figure 3b–d. In the case of LiYF$_4$:Pr^{3+}, the energy donor is a Praseodymium ion in the upper-level $^3P_0$ and the energy acceptor is a Praseodymium ion in the ground level $^3H_4$. Accordingly, two ions in levels ($^3P_0$, $^3H_4$) enter levels ($^3H_4$, $^3P_0$), see Figure 3b. Since the sum of energy in the $^3P_0$ level does not change through this energy transfer we consider it energy-conserving.

Energy transfer between ions with complex energy level schemes can include intermediate energy levels resulting in well-known upconversion or cross-relaxation. In the case of LiYF$_4$:Pr^{3+}, two cross-relaxation processes are prominent and involve two ions in levels ($^3P_0$, $^3H_4$) that either enter the levels ($^3H_6$, $^1D_2$) or ($^1G_4$, $^1G_4$), compare Figure 3c,d.[44,45] Even though this process conserves the sum of the excitation energy in a nanoparticle, we consider it lossy, because it depopulates the upper $^3P_0$ level. The energy transfer rates only differ by the spectral overlap of the involved transitions. Therefore, the characteristic lengths for the lossy cross-relaxations and conserving energy transfer can be related to each other by a ratio of the overlap spectra, see Supporting Information for a detailed mathematical description.

Besides spontaneous emission and cross-relaxations, multiphonon quenching can depopulate the upper $^3P_0$ level, see Figure 3e. Although this process is highly unlikely in bulk crystals, as the low phonon energy of 480 cm^{-1} requires at least 7 phonons this process gains relevance in the case of nanoparticles. Since they are typically dispersed in organic solvents, which exhibit higher vibration energies, these solvents allow lower-order multiphonon interaction. Here, we used toluene as a solvent and oleic acid as a ligand that both accept vibration energies of the C-H bonds of up to ca. 3000 cm^{-1}.[46,47] The energy difference between the $^3P_0$ and $^1D_2$ lies in that same order of magnitude consequently allowing for a single phonon transition. As a result, LiYF$_4$:Pr^{3+} nanoparticles exhibit an additional emission line at 595 nm originating from the $^1D_2$ level populated via the efficient multiphonon quenching pathway.[22]

Multiphonon quenching is also a form of Förster energy transfer with the organic solvent acting as energy acceptor.[48] Consequently, multiphonon quenching, as an energy transfer mechanism, depends on a characteristic length mainly determined by the spectral overlap of the involved transitions. This length can be calculated in principle, but the single input parameters strongly depend on the experimental conditions.[49] As these conditions are unknown simple calculations to obtain the characteristic lengths are not possible. We identified the characteristic lengths by comparison between experimentally and numerically determined excited state lifetimes. The lifetime acts as the main control parameter and as such is accompanied by the quantum yield.

2.2. Monte Carlo Simulation

To model the spatiotemporal dynamics inside the nanoparticles, we considered a Monte Carlo approach, summarized by the flow chart in **Figure 4**. Prior to a simulation run, we need to specify the geometry and number of ions. These form the sole parameters required to simulate the excitation dynamics of a nanoparticle. Note that we can reduce the complexity of the nanoparticles, that is, the energy level scheme in the numerical model to allow for considerable lower computation durations. Nevertheless, the considered approach allows taking into account all Pr^{3+} energy levels. Consequently, energetically more complex nanoparticle systems such as upconversion particles can as well be treated within the considered approach as long as the necessary spectroscopic information is available.
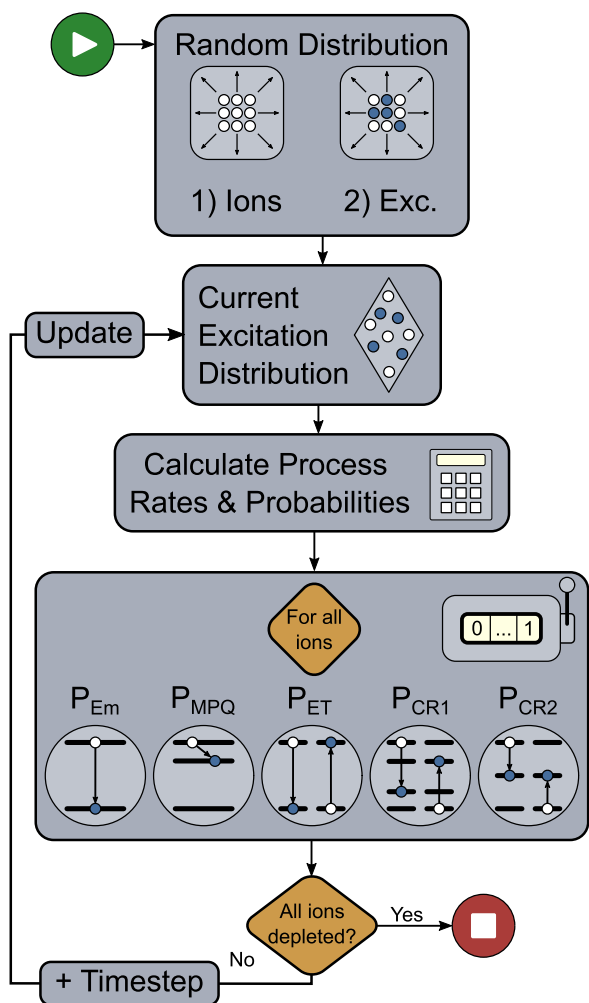
**ADVANCED
SCIENCE NEWS**

www.advancedsciencenews.com

**ADVANCED
OPTICAL
MATERIALS**

www.advopticalmat.de

Figure 4. Flow chart of the Monte Carlo approach detailed in the main text. After randomly distributing the ions and the excitation energy we decide which process will occur for every ion based on probabilities and repeat this for as many timesteps as necessary to deplete all ions.

Our Monte Carlo approach follows the subsequent steps: At the start, we randomly distribute the ions within a nanoparticle of a given dimension. For this purpose, a database is created that contains one entry for every given ion. In this entry, the position of the ion is stored as a 3D coordinate. We assign each ion a flag for every involved process and initialize the flags to zero.

Second, we distribute the excitation randomly within the available ions. To achieve this, we set the excitation flag of randomly chosen ions to one. We set the maximum excitation density to 50% which allows us to neglect stimulated emission.

After calculating the process rates, we determine the probability for each process to occur. This is based on probability theory considerations; interested readers find the details in Supporting Information.

In the main part, we determine the actual process that is to occur. For every ion, we first calculate the process rates and from that the probability for every process. Next, one random variable between zero and one is generated (machine precision) and compared to the process probabilities to decide what hap-

pens. In the case of spontaneous emission, we set the excitation flag of the current ion to zero. For energy transfer, we set the flag of the current ion to zero and the flag of the respective adjacent ion to one. The levels involved in cross-relaxation, $^1G_4$ and $^3H_6$, are known to exhibit lifetimes in the range of several milliseconds.[50–52] Since these lifetimes exceed the simulation window of $300\,\mu s$ by around one order of magnitude, we consider the energy trapped in these levels during the further simulation. Respective ions are excluded from interaction with other ions or the surrounding medium. However, the situation is different for processes that involve the $^1D_2$ level. Our previous work revealed that emission from this level plays a special role in the spectroscopy of LiYF$_4$:Pr^{3+} nanoparticles. Therefore, we implemented spontaneous emission from that level in the numerical model. Once the processes have been chosen for every ion the process flags are stored as part of the process statistics for later post-processing. A timestep of $20\,ns$ is added and the process restarts for the updated excitation distribution.

Once all ions are depleted the process statistics and spatial information of the excitation dynamics are returned.

Before determining the characteristic lengths, we simulated the particles of the concentration series with arbitrary parameters and repeated the simulations to determine the statistical deviation. In **Figure 5**a, we depict the standard deviations of the simulated excited state lifetimes for an increasing number of simulations. The depicted relation matches the expected $1/\sqrt{N}$ trend: For a total of $N = 100$ simulations, the standard deviation amounts to 20 to 40% depending on the sample. For $N = 1000$ simulations, this deviation decreases to 10 to 15% and finally to 2 to 3% for $N = 10\,000$.

We scanned the 3D parameter space to obtain the characteristic lengths. For that, we started with $N = 100$ simulations and broad parameter ranges of (0.1–8 nm, 2–20 Å, 0.1–11 nm) at a scanning resolution of (1 nm, 2 Å, 1 nm) for multiphonon quenching (MPQ), Dexter energy transfer (DET), and Förster energy transfer (FET), respectively. To gradually narrow down this parameter space, we iteratively increased both, the number of simulations and the resolution of the parameters (see Figure 5b). In this way, we obtained more precise results as we approached the actual parameters.

To extract information from the parameter scans, we averaged the simulated lifetimes in two dimensions of the parameter space for all four samples of the concentration series and plotted the result as a function of the remaining parameter. To further narrow down the relevant parameter space we iteratively reduced the averaging window in the two dimensions. This procedure was limited by simulation accuracy and resolution of the parameter steps. For the first scan, we fitted a polynomial of 6th order as well as an exponential function to the numerical results of the Förster and Dexter energy transfer-related processes, respectively. This served as a first cross-check for the validity of the simulations because these analytical functions govern the respective processes. For the first iteration, we chose those parameters which deviated around ±30% from the average measured values and analyzed $N = 1000$ independent instances with a resolution of (0.5 nm, 1 Å, 0.5 nm) for multiphonon quenching, Dexter and Förster energy transfer, respectively. The results correlate linearly, consequently, we fitted linear functions which yielded coefficients of determination close to one. To determine the first set of the
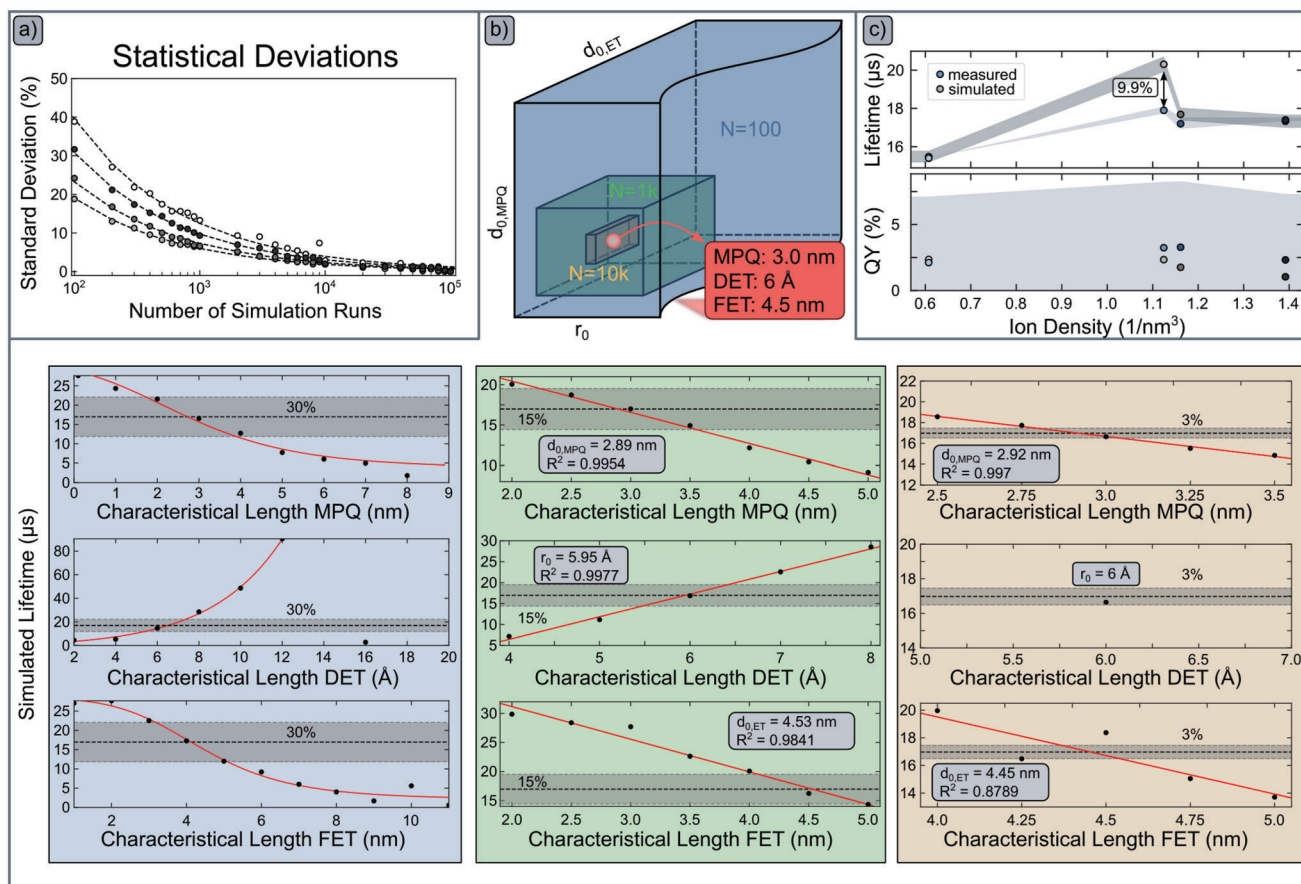
**ADVANCED
SCIENCE NEWS**

www.advancedsciencenews.com

**ADVANCED
OPTICAL
MATERIALS**

www.advopticalmat.de

Figure 5. Determination of the characteristic lengths. a) The standard deviation of the simulations decreases by $1/\sqrt{N}$ with the number of simulation runs N as expected from a simple sampling Monte Carlo approach. The numerical error is determined from this plot. b) Graphical representation of the parameter search: To find the parameters in the 3D parameter space we applied an iterative algorithm that increases resolution and numerical certainty at the cost of a broader scanning range. The indicated 30%, 15%, and 3%, respectively, represent the expected standard deviation of the simulated data and limit the accepted parameter range. c) Comparison of the experimental figure-of-merit with the simulated results obtained with the parameters from the characteristic length determination. Note that the markers represent the samples of the concentration series.

characteristic lengths, we calculated the intersection between the linear functions and the averaged value from the measurement. For improved accuracy, we simulated parameters that deviated only around ±15% from the average measured excited state lifetime. From this last parameter scan, we identified the characteristic lengths to be (3 nm, 6 Å, 4.5 nm) for multiphonon quenching, Dexter, and Förster energy transfer, respectively.

We obtained the characteristic lengths by including the measured excited state lifetime of the $^1D_2$ level in the simulations. To check for the potential to further simplify the energy level scheme and remove irrelevant processes we repeated the last parameter scan with different $^1D_2$ lifetimes, see Supporting Information for details. Finally, we obtained parameters that deviated by less than 7% from the initial scan by neglecting emission from the $^1D_2$ level. Consequently, we decided to continue the simulations with this less complex model.

We simulated the samples of the concentration series with the identified characteristic lengths for verification and found the numerical results to match the experimental value extraordinarily well. As evident from Figure 5c, the maximum deviation of simulation and measurement amounts to only 10%, taking into ac-

count the numerical and experimental errors of the excited state lifetime. For the quantum yield, this deviation can not be determined due to the large experimental measurement error.

2.3. Prediction of the Excitation Dynamics

Combining the identified characteristic lengths with the numerical model, we were able to predict the excited state lifetimes of the size series with a maximum deviation of only 12.6%. These samples were not involved in determining the characteristic lengths. Furthermore, the ion density of these samples is one order of magnitude greater than that for the concentration series. We conclude that these simulations verify and validate the numerical model.

Below ion densities of 8.5 ions nm^{-3}, the simulation and measurement agree within the respective uncertainties, see **Figure 6**a. Above this value, the deviation increases. The simulated lifetimes get increasingly smaller than the measured lifetime for increasing ion numbers. As evident from Figure 6b, interionic energy transfer, that is, cross relaxations, are dominant at these
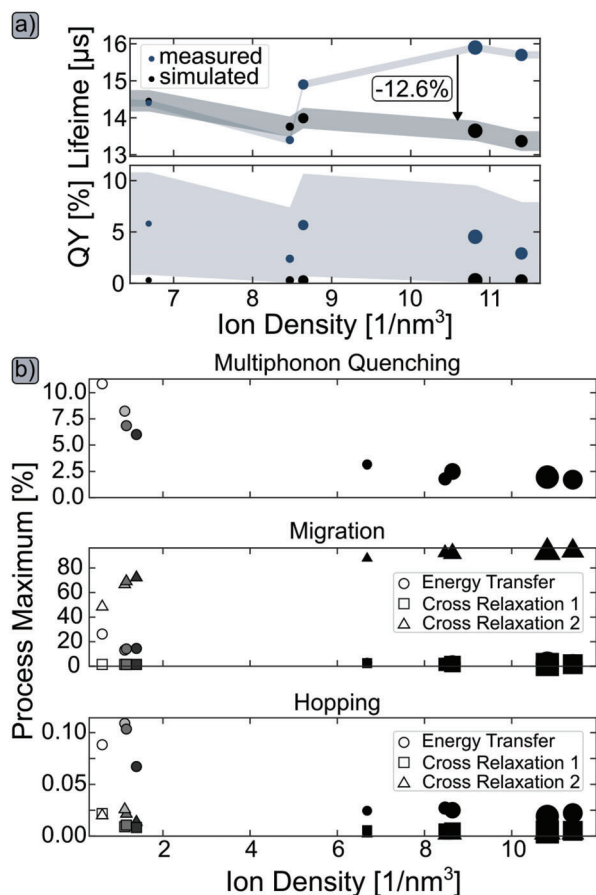
**ADVANCED
SCIENCE NEWS**

www.advancedsciencenews.com

**ADVANCED
OPTICAL
MATERIALS**

www.advopticalmat.de

Figure 6. a) Measured and simulated lifetime and quantum yield of the size series. The numerical model predicts the spectroscopic performance of these samples. b) The process statistics of all samples exhibit that multiphonon quenching decreases with the nanoparticle size, and concentration quenching drastically limits the performance of the nanoparticles.

Figure 7. Numerical results on core-shell particles. a) Schematic of the core-shell particles with a shell thickness of 6 nm. b) The shell drastically increases the excited state lifetime by a maximum of 44 % and also improves the quantum yield by 3.5 percentage points. c) The shell suppresses multi-phonon quenching. The performance of such nanoparticles is limited through concentration quenching.

ion densities. The respective cross-relaxation transfer involves the $^1G_4$ level (see Figure 1) that, in principle, can take part in upconversion.[45] However, upconversion from the $^1G_4$ to the $^3P_0$ level is not considered in the model we employed but could contribute to the elongation of the excited state lifetimes. In this case, the $^1G_4$ level serves as an energy reservoir that releases its energy to the $^3P_0$ level after a certain time and, like this, contributes to elongated lifetimes. If future investigations need an increased level of accuracy for 5 at% doped nanoparticles this process can readily be added to the numerical approach. Since here we aim to demonstrate the capabilities of our numerical approach for the first time we consider the accuracy acceptable. For the quantum yield of the size series, we observed a broad underground in the emission spectra of the nanoparticles during the measurement that might originate from oleic acid content.[22] This underground could not be readily removed from the measurement. Therefore, we estimate the real experimental quantum yield to be at least 1% lower than the values depicted in Figure 6a. Due to the comparatively large experimental error, the true deviation is again difficult to determine.

We analyzed the process statistics to gain a deeper insight into the excitation dynamics inside the nanoparticles, see Fig-
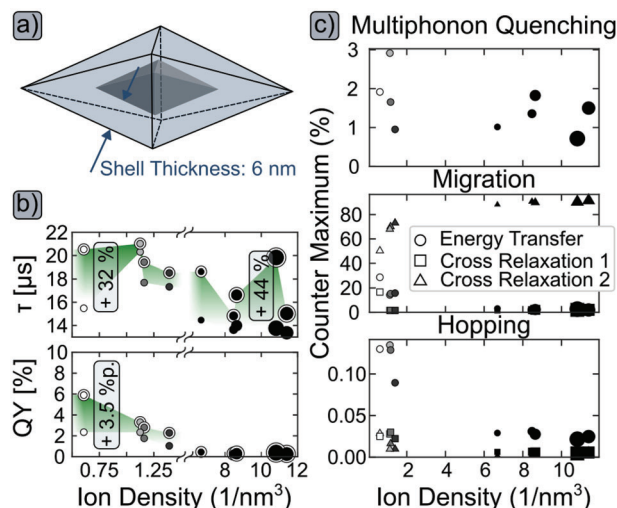
ure 6b. Interestingly, those processes dominating the excitation dynamics start at a high level and drastically decrease within the first microsecond, see Figures S12–S20 (Supporting Information). However, the relative process maxima vary for the different samples as depicted in Figure 6b. The multiphonon quenching shows a maximum of around 10% for low ion densities and decreases with higher ion density. This is plausible since the nanoparticle volume increases and approaches bulk-like situations in which the surface-to-bulk-ion ratio decreases and thus reduces the importance of multiphonon quenching to the surrounding medium. In the simulations, hopping processes are negligible with relative process maxima well below 1%, the migration processes strongly influence the dynamics. Migrating energy transfer decreases with the ion density at the cost of an increase in migrating cross-relaxation. This is comprehensible as concentration quenching is known to increase for high doping concentrations.[30] Furthermore, the decrease in the multiphonon quenching coincides with the decrease in the migrating energy transfer. We infer that energy migrates to the surface of the nanoparticles where the quenching occurs. This process loses relevance with increasing ion density as concentration quenching becomes more dominant.

2.4. A Simple Numerical Optimization Approach

As first main advantage, our simulation approach enables the numerical optimization of lanthanide nanoparticles. To demonstrate this potential, we added an inert shell around all nanoparticles in the model and repeated the simulations, see **Figure 7**a. Adding a neutral shell around doped core particles is a common and well-known strategy to suppress energy loss via multiphonon quenching and thus improve the performance of lanthanide nanoparticles.[53–60] However, this numerical optimization step is only possible because our modelling approach

**ADVANCED
SCIENCE NEWS**

www.advancedsciencenews.com

**ADVANCED
OPTICAL
MATERIALS**

www.advopticalmat.de

accounts for the spatial distribution enabling to simulate the underlying surface effects. Based on simple estimations, it is evident that the efficiency of the dipole-dipole interaction decreases to 1.5% if the distance between the energy donor and acceptor is twice the characteristic length. Therefore, we chose a shell thickness of 6 nm which is twice the characteristic length that the parameter search revealed.

The neutral shell led to a drastic increase in the excited state lifetime. The lifetime of the concentration and size series increased by 32% and 44%, respectively, with a maximum of above 20 μs. On the other hand, the quantum yield increases to a maximum of 6%. This is only one percentage point above our current measurement uncertainty. Furthermore, the increase of the quantum yield strongly depends on the ion density and becomes vanishingly small at densities above one ion per nm³, see Figure 7b.

We again analyzed the process statistics to gain deeper insights into the underlying mechanisms. As in the case of the core particles, those processes that dominate the excitation dynamics start at a high level and drastically decrease within the first microsecond, see Figures S21–S29 (Supporting Information). Again, however, the relative process maxima vary for the different samples as depicted in Figure 7b. The shell reduces multiphonon quenching by a factor of approximately 5. We infer that this reduction allows for the higher simulated excited state lifetimes.[55–60] Since the further processes show no significant deviation from the core-only particles we infer that in core-shell particles concentration quenching via cross relaxations is the limiting process and prevents high quantum yields as already known from bulk crystals.[30,31]

Besides the scientific potential, these results illustrate the enormous resource-related potential of our numerical approach: Approaching the strategy of adding a shell around lanthanide nanoparticles includes (i) the synthesis of the core particles and growing the shell, (ii) the structural characterization (TEM, EDX, XRD, etc.), and (iii) the optical characterization (lifetimes and quantum yield). In the present case, we replaced this effort with the simulations and saved respective resources.

2.5. Spatial Excitation Dynamics

As second main advantage, our simulation approach enables the spatiotemporal analysis of the dynamics within nanoparticles. To highlight this advantage, we simulated single core-only as well as core-shell particles and calculated the average distance of the excitation energy from the center of the nanoparticles, see **Figure 8**.

Independent of the structural characteristics, energy seems to move toward the surface of the nanoparticles, even in the case of core-shell structures. This is indeed an interesting observation, but one has to keep in mind that these results only depict the spatial energy movement in one single nanoparticle.

Nonetheless, it is noteworthy that some of the nanoparticles exhibit oscillations of the average energy position, see the insets in Figure 8. These oscillations point toward a special type of energy trapping where energy transfer occurs so fast that no competing loss mechanism can extract the energy from the nanoparticle. We observed these oscillations only for nanoparticles from the concentration series and, therein, only for the two samples
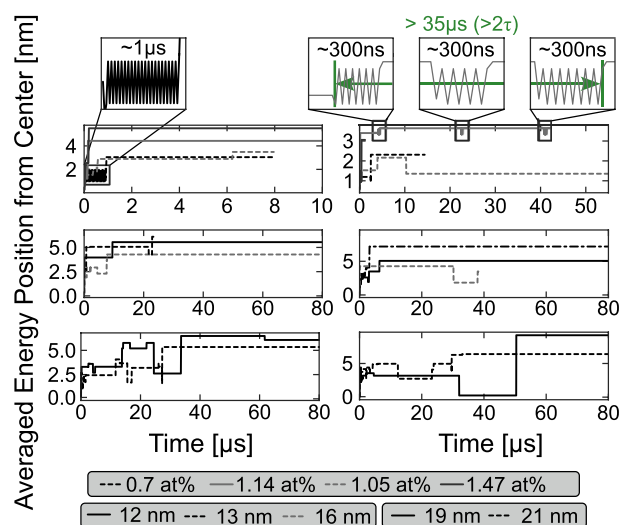

Figure 8. Spatial analysis of single particles consisting of core-only (left) and core-shell (right): Energy tends to move toward the particle surface and that some ion pairs seem to act as oscillating energy traps.

with the lowest number of ions. The longest continious oscillation lasted for about 1 μs (6% of the lifetime) and took place between 1 nm and 2 nm from the center of the respective nanoparticle. However, we also observed a series of short-timed oscillations (ca. 300 ns, 1.5% of the lifetime) within one nanoparticle that were interrupted by periods of stagnation at one position. This whole series lasted about 35 μs, which is in the order of magnitude of the bulk crystal's lifetime,[29] and took place about 3.5 nm from the center of the nanoparticle. Remarkably, the energy has been trapped in this individual nanoparticle for more then twice the lifetime determined in the experiments and simulations. We speculate that such an effect can be exploited to drastically increase the spontaneous emission lifetime or to store information within nanoparticles. However, more detailed conclusions require multiple simulations and an in-depth analysis which are out of the scope of the present work. At the same time, the experimental demonstration of these effects will pose a great challenge which emphasizes the strengths of our model.

3. Conclusion

Numerical simulations on the excitation dynamics in lanthanide nanoparticles contribute to a deeper understanding of these processes. They carry the potential to enable the numerical optimization of nanoparticles and reveal new spatiotemporal effects. Current approaches are based on rate equations and spatially limited because they employ an averaging model that cannot account for single ions. These approaches origin from the modeling of laser active bulk crystals and, consequently, play a minor role in nanoparticle research. We developed a flexible and versatile numerical model that is not subject to any limitation and therefore has enormous potential. Our model is based on a Monte Carlo approach and implemented in a modular manner allowing us to flexibly add or remove physical processes and energy levels, including nanoparticles with custom geometries. Consequently, it is universally applicable to all types of lanthanide nanoparticles.

**ADVANCED
SCIENCE NEWS**

www.advancedsciencenews.com

**ADVANCED
OPTICAL
MATERIALS**

www.advopticalmat.de

We employed a model of LiYF$_4$:Pr^{3+} and fitted it to the measured values of a concentration series ($\approx$10 nm and 0.7–1.47 at%) of the respective nanoparticles. We could reproduce the excitation dynamics of this concentration series and, with a maximum deviation of 12.6%, reliably predict the lifetimes and quantum yields of size series ($\approx$5 at% and 12–21 nm) that was not included in the parameter search. Our model allows us to trace the spatiotemporal excitation and de-excitation routes and thus provides a deeper insight into the excitation dynamics enabling numerical optimization of the nanoparticles. We illustrated that by simulating the nanoparticles with a neutral shell which, as expected, drastically increased the excited state lifetime and took a maximum of 5% of the time necessary for an experimental optimization. We demonstrated the potential of our approach by performing a spatial analysis of the excitation dynamics in single nanoparticles and found oscillations that point toward a new type of energy trapping.

Altogether, our numerical model is a powerful tool for understanding, predicting, and optimizing lanthanide nanoparticles regarding their spatio-temporal spectroscopic properties. We plan to further optimize LiYF$_4$:Pr^{3+} nanoparticles numerically toward high excited state lifetimes and quantum yields and to verify the optimization with further experiments. We anticipate that the optimization process might yield novel particle designs with tailored spectroscopic properties which will induce interesting new challenges for synthesists. This numerical optimization will challenge synthesists to improve synthesis routes for manufacturing such optimized particles, even for other lanthanide nanomaterials such as upconversion or photoavalanching nanoparticles toward high performance.

4. Experimental Section

Synthesis and Structural Characterization of LiYF$_4$:Pr^{3+} Doped Nanoparticles: The synthesis of monodisperse LiYF$_4$:Pr^{3+} nanoparticles downsized to 10 nm was reported in the previous work.[22] During synthesis, the optimum amount of oleic acid in combination with the right heating temperature and duration plays a crucial role to obtain high-quality LiYF$_4$:Pr^{3+} nanoparticles. For a detailed description, an appropriate amount of YCl$_3$ and PrCl$_3$ (each 99.9%, Sigma Aldrich) in methanol was mixed with oleic acid and octadecene (both 20 ml and technical grade, Alfa Aesar) in a three-necked round bottom flask. The flask was connected to a reflux condenser, a temperature sensor, and a septum resulting in a modified Schlenk-line setup. The mixture was stirred and heated to 170 °C for 30 min under N$_2$ atmosphere and then cooled down to 50 °C. Next, the mixture was degassed at 100 °C in a vacuum (<1 mbar). Afterward, LiOH (3 mmol, 99.995%, Sigma Aldrich) was added under N$_2$ flow and then stirred under vacuum for another 30 min. Subsequently, 12 mmol NH$_4$F (99.99%, Sigma–Aldrich) was added and the mixture was heated up to 300 °C for 90 min. After cooling below 30 °C the mixture was precipitated with 1:1 addition of ethanol and centrifuged for collection. The residue was redispersed in toluene (10 ml, 99.8%, Sigma–Aldrich). If necessary, the washing step was repeated and finally, the precipitated nanoparticles were redispersed in toluene (5 ml). The ratio and amount of YCl$_3$ and PrCl$_3$ were tuned to obtain the different praseodymium doping concentrations while the LiOH content was tuned to obtain different sizes.

50 μl of the obtained dispersions were dried on a Si wafer and analyzed in an X-ray diffractometer (PANalytical X'PERT Pro) equipped with a Cu Kα X-ray source (154 pm). The analysis revealed a tetragonal crystal lattice with space group I4$_1$/a with unit cell parameters $a = 5.171$ Å and $c = 10.748$ Å as well as a density of 3.96 g cm^{-3}. 10 μl of the dispersions were dried on a copper grid and electron microscope pictures were taken in a TEM (JEOL JEM-1011) operated at 100 kV. An EDX spectrometer (JEOL JEM 2200 FS, FEG cathode, 200 kV, Oxford X-Max 100TLE, SDD 100 mm^3) attached to the TEM was used to take electron spectra of at least three different areas for the elemental content analysis of the nanoparticles. Detailed results of the structural characterization are presented in the supporting information, see Figures S1–S10 (Supporting Information).

Optical Spectroscopy: Cuvettes filled with the dispersions were used to measure the excited state lifetimes and quantum yields. The lifetimes were obtained from an in-house built setup. A flashlamp pumped q-switched Nd:YAG laser (Spectra Physics Quanta Ray GCR-170) delivering 10 ns pulses at 1064 nm with up to 1 J pulse energy at 10 Hz repetition rate was frequency tripled to pump an optical parametrical oscillator (OPO, GWU ULD-240). Light from the OPO was focused into the cuvettes with an lens ($f = 500$ mm, Thorlabs). The OPO was tuned to 479 nm to excite the nanoparticles from the ground level $^3H_4$ to the $^3P_0$ level, and a maximum excitation energy of 5 mJ was set to obtain sufficient signal to record the spontaneous emission decay. The emission was collected with a parabolic mirror (3 in., Thorlabs) and then focused into a monochromator (M150, Solar Laser Systems) using high numerical aperture lenses (Thorlabs). The monochromator was tuned to the emission wavelength of interest, and a Silicium photodiode with an integrated gain module (100 MHz, Femto OE-300-SI-30) was attached as a detector. The photodiode was connected to an oscilloscope (500 MHz, 2.5 GSa s^{-1}, 50 Ω; Tektronix 620B) that was read out by a computer via GPIB-to-USB connection. An average of 100 measurements was sufficient to reduce noise and eliminate the influence of energy fluctuations of the excitation pulses. The obtained signal consisted of three exponential signals which were assigned to the residual excitation light, emission from oleic acid ligands, and the desired emission from the nanoparticles. The lifetimes were obtained by applying a sophisticated fitting routine which we reported in our previous work.[22]

The quantum yield was obtained using a photoluminescence spectrometer (Edinburgh Instruments) with an integrated integration sphere. Absolute absorption and emission spectra were taken from a cuvette filled with the nanoparticle dispersion as well as a reference cuvette filled with the solvent (toluene) only at a spectral resolution of 1 nm. The absorption and emission spectra of the sample and the reference were integrated and the reference value was subtracted from the sample value. Finally, the quantum yield was obtained from the ratio of these values.

An exemplary spectra of the spontaneous emission is provided in Figure S30 (Supporting Information) and more details on the absorption and emission spectroscopy of LiYF$_4$:Pr^{3+} nanoparticles can be found in our previous work.[22]

Software: We implemented the numerical model based on a Monte Carlo approach in Python 3. The program only needs the NumPy module (version > 1.18.4) for operation. Additionally, the ABC module is used to enable abstract base classes.

Computation: We run simulations on a scientific computing cluster with 80 nodes. Each node consisted of two Intel Cascade Lake Xeon Gold 6230N 2.3 GHz CPUs with 20 cores per CPU (40 cores per node, 3200 cores in total). A total memory of 192 GB was available per node. The cluster is managed through the SLURM workload manager. The simulations were parallelized to make use of the available computing resources. While simulations with $N_{Ions} < 50$ and $N_{Rep} = 100$ repetitions took only 5 to 10 min per task more costly simulations with $N_{Ions} < 1k$ and $N_{Rep} = 10k$ took more than 24 h. For the simulation of one single core-shell nanoparticle, a maximum of 100 cores was employed parallelly resulting in a time consumption of 48 h at maximum. Running such a simulation on a personal computer with, for example, 6 cores would be feasible. However, this would take 40 days (assuming that one core is needed to run the operating system). Total storage of 100 GB was available and well used since files containing the process statistics easily exceeded 10 GB for one sample.

Supporting Information

Supporting Information is available from the Wiley Online Library or from the author.

**ADVANCED
SCIENCE NEWS**

www.advancedsciencenews.com

**ADVANCED
OPTICAL
MATERIALS**

www.advopticalmat.de

Conflict of Interest

The authors declare no conflict of interest.

Author Contributions

S.S., J.T., and A.R. developed the numerical model. O.M. and A.D. implemented the modular core of the program. S.S. extended the program according to the experimental boundary conditions. R.K. and C.G. performed the synthesis and structural analysis of the samples. S.S. performed the experimental and numerical investigation that were analyzed by S.S., J.T., D.R., and A.R. S.S. wrote the manuscript with input from all co-authors. All authors approved the final version of the manuscript.

Data Availability Statement

The data that support the findings of this study are available from the corresponding author upon reasonable request.

[1] O. Svelto, D. C. Hanna, *Principles of Lasers*, Plenum Press, New York, **1998**.

[2] X. Qin, X. Liu, W. Huang, M. Bettinelli, X. Liu, *Chem. Rev.* **2017**, *117*, 4488.

[3] T. Zhong, P. Goldner, *Nanophotonics* **2019**, *8*, 2003.

[4] F. Vetrone, R. Naccache, A. Zamarrón, A. Juarranz de la Fuente, F. Sanz-Rodríguez, L. Martinez Maestro, E. Martín Rodriguez, D. Jaque, J. García Solé, J. A. Capobianco, *ACS Nano* **2010**, *4*, 3254.

[5] P. Netzsch, M. Hämmer, E. Turgunbajew, T. P. van Swieten, A. Meijerink, H. A. Höppe, M. Suta, *Adv. Opt. Mater.* **2022**, *10*, 2200059.

[6] J. Hu, D. H. Ortgies, E. Martín Rodríguez, F. Rivero, R. Aguilar Torres, F. Alfonso, N. Fernández, G. Carreño-Tarragona, L. Monge, F. Sanz-Rodriguez, M. d. C. Iglesias, M. Granado, A. L. García-Villalon, J. García Solé, D. Jaque, *Adv. Opt. Mater.* **2018**, *6*, 1800626.

[7] B. del Rosal, A. Pérez-Delgado, E. Carrasco, D. J. Jovanović, M. D. Dramićanin, G. Dražić, n. J. de la Fuente, F. Sanz-Rodriguez, D. Jaque, *Adv. Opt. Mater.* **2016**, *4*, 782.

[8] F. Carl, L. Birk, B. Grauel, M. Pons, C. Würth, U. Resch-Genger, M. Haase, *Nano Res.* **2021**, *14*, 797.

[9] J. Liao, J. Zhou, Y. Song, B. Liu, Y. Chen, F. Wang, C. Chen, J. Lin, X. Chen, J. Lu, D. Jin, *Nano Lett.* **2021**, *21*, 7659.

[10] L. Tu, X. Liu, F. Wu, H. Zhang, *Chem. Soc. Rev.* **2015**, *44*, 1331.

[11] X. Liu, R. Deng, Y. Zhang, Y. Wang, H. Chang, L. Huang, X. Liu, *Chem. Soc. Rev.* **2015**, *44*, 1479.

[12] H. Dong, L.-D. Sun, C.-H. Yan, *Chem. Soc. Rev.* **2015**, *44*, 1608.

[13] G. Liu, *Chem. Soc. Rev.* **2015**, *44*, 1635.

[14] G. Chen, H. Ågren, T. Y. Ohulchanskyy, P. N. Prasad, *Chem. Soc. Rev.* **2015**, *44*, 1680.

[15] Z. Wang, A. Meijerink, *J. Phys. Chem. C* **2018**, *122*, 26298.

[16] A. E. Siegman, *Lasers*, University Science Books, New York, **1986**.

[17] M. Dudek, M. Szalkowski, M. Misiak, M. Ćwierzona, A. Skripka, Z. Korczak, D. Piątkowski, P. Woźniak, R. Lisiecki, P. Goldner, S. Maćkowski, E. M. Chan, P. J. Schuck, A. Bednarkiewicz, *Adv. Opt. Mater.* **2022**, *10*, 2201052.

[18] R. B. Anderson, S. J. Smith, P. S. May, M. T. Berry, *J. Phys. Chem. Lett.* **2014**, *5*, 36.

[19] M. Y. Hossan, A. Hor, Q. Luu, S. J. Smith, P. S. May, M. T. Berry, *J. Phys. Chem. C* **2017**, *121*, 16592.

[20] G. Tessitore, G. A. Mandl, M. G. Brik, W. Park, J. A. Capobianco, *Nanoscale* **2019**, *11*, 12015.

[21] J. W. Stouwdam, G. A. Hebbink, J. Huskens, F. C. J. M. van Veggel, *Chem. Mater.* **2003**, *15*, 4604.

[22] R. Komban, S. Spelthann, M. Steinke, D. Ristau, A. Ruehl, C. Gimmler, H. Weller, *Nanoscale Adv.* **2022**, *4*, 2973.

[23] F. T. Rabouw, P. T. Prins, P. Villanueva-Delgado, M. Castelijns, R. G. Geitenbeek, A. Meijerink, *ACS Nano* **2018**, *12*, 4812.

[24] P. Villanueva-Delgado, K. W. Krämer, R. Valiente, *J. Phys. Chem. C* **2015**, *119*, 23648.

[25] P. Villanueva-Delgado, K. W. Krämer, R. Valiente, M. de Jong, A. Meijerink, *Phys. Chem. Chem. Phys.* **2016**, *18*, 27396.

[26] F. Pini, L. Francés-Soriano, N. Peruffo, A. Barbon, N. Hildebrandt, M. M. Natile, *ACS Appl. Mater. Interfaces* **2022**, *14*, 11883.

[27] C. Lee, E. Z. Xu, Y. Liu, A. Teitelboim, K. Yao, A. Fernandez-Bravo, A. M. Kotulska, S. H. Nam, Y. D. Suh, A. Bednarkiewicz, B. E. Cohen, E. M. Chan, P. J. Schuck, *Nature* **2021**, *589*, 230.

[28] S. Y. Kim, J. S. Jeong, K. A. Mkhoyan, H. S. Jang, *Nanoscale* **2016**, *8*, 10049.

[29] A. Richter, E. Heumann, G. Huber, V. Ostroumov, W. Seelert, *Opt. Express* **2007**, *15*, 5172.

[30] A. Richter, E. Heumann, E. Osiac, G. Huber, W. Seelert, A. Diening, *Opt. Lett.* **2004**, *29*, 2638.

[31] N.-O. Hansen, A.-R. Bellancourt, U. Weichmann, G. Huber, *Appl. Opt.* **2010**, *49*, 3864.

[32] P. W. Metz, F. Reichert, F. Moglia, S. Müller, D.-T. Marzahl, C. Kränkel, G. Huber, *Opt. Lett.* **2014**, *39*, 3193.

[33] W. B. nos, G. Brasse, F. Starecki, A. Braud, J.-L. Doualan, R. Moncorgé, P. Camy, *Opt. Lett.* **2014**, *39*, 4450.

[34] M. Gaponenko, P. W. Metz, A. Härkönen, A. Heuer, T. Leinonen, M. Guina, T. Südmeyer, G. Huber, C. Kränkel, *Opt. Lett.* **2014**, *39*, 6939.

[35] C. Kränkel, D.-T. Marzahl, F. Moglia, G. Huber, P. W. Metz, *Laser Photonics Rev.* **2016**, *10*, 548.

[36] K. Dolgaleva, R. W. Boyd, P. W. Milonni, *J. Opt. Soc. Am. B* **2007**, *24*, 516.

[37] K. Dolgaleva, R. W. Boyd, *J. Opt. Soc. Am. B* **2007**, *24*, A19.

[38] K. K. Pukhov, T. T. Basiev, Y. V. Orlovskii, *JETP Lett.* **2008**, *88*, 12.

[39] T. Förster, *Ann. Phys.* **1948**, *437*, 55.

[40] D. L. Dexter, *J. Chem. Phys.* **1953**, *21*, 836.

[41] R. Deng, J. Wang, R. Chen, W. Huang, X. Liu, *J. Am. Chem. Soc.* **2016**, *138*, 15972.

[42] X. Chen, L. Jin, W. Kong, T. Sun, W. Zhang, X. Liu, J. Fan, S. F. Yu, F. Wang, *Nat. Commun.* **2016**, *7*, 10304.

[43] M. Inokuti, F. Hirayama, *J. Chem. Phys.* **1965**, *43*, 1978.

[44] M. Fibrich, J. Šulc, H. Jelínková, *Laser Phys. Lett.* **2015**, *12*, 095801.

[45] R. Naccache, F. Vetrone, A. Speghini, M. Bettinelli, J. A. Capobianco, *J. Phys. Chem. C* **2008**, *112*, 7750.

[46] J. K. Wilmshurst, H. J. Bernstein, *Can. J. Chem.* **1957**, *35*, 911.

[47] I. W. Schie, L. Nolte, T. L. Pedersen, Z. Smith, J. Wu, I. Yahiaténe, J. W. Newman, T. Huser, *Analyst* **2013**, *138*, 6662.

[48] V. L. Ermolaev, E. B. Sveshnikova, E. N. Bodunov, *Physics-Uspekhi* **1996**, *39*, 261.

[49] P. A. Tanner, L. Zhou, C. Duan, K.-L. Wong, *Chem. Soc. Rev.* **2018**, *47*, 5234.

[50] B. M. Walsh, U. Hommerich, A. Yoshikawa, A. Toncelli, *J. Lumin.* **2018**, *197*, 349.

[51] P. Wu, B. Xiao, Q. Feng, X. Lin, W. Li, H. Xu, Z. Cai, *J. Lumin.* **2021**, *235*, 118028.

[52] Z. Wang, Z. Dai, S. Ji, S. Huang, B. Xiao, Z. He, H. Xu, Z. Cai, *J. Lumin.* **2022**, *247*, 118870.

[53] F. Vetrone, R. Naccache, V. Mahalingam, C. G. Morgan, J. A. Capobianco, *Adv. Funct. Mater.* **2009**, *19*, 2924.

[54] J. Zhao, X. Chen, B. Chen, X. Luo, T. Sun, W. Zhang, C. Wang, J. Lin, D. Su, X. Qiao, F. Wang, *Adv. Funct. Mater.* **2019**, *29*, 1903295.

[55] C. Würth, S. Fischer, B. Grauel, A. P. Alivisatos, U. Resch-Genger, *J. Am. Chem. Soc.* **2018**, *140*, 4922.

[56] R. Ghosh Chaudhuri, S. Paria, *Chem. Rev.* **2012**, *112*, 2373.

[57] X. Chen, D. Peng, Q. Ju, F. Wang, *Chem. Soc. Rev.* **2015**, *44*, 1318.

[58] F. Wang, R. Deng, J. Wang, Q. Wang, Y. Han, H. Zhu, X. Chen, X. Liu, *Nat. Mater.* **2011**, *10*, 968.

[59] P. Ren, X. Zheng, J. Zhang, S. De Camillis, J. Jia, H. Wang, X. Liao, J. A. Piper, Y. Lu, *ACS Photonics* **2022**, *9*, 758.

[60] A. D. Ostrowski, E. M. Chan, D. J. Gargas, E. M. Katz, G. Han, P. J. Schuck, D. J. Milliron, B. E. Cohen, *ACS Nano* **2012**, *6*, 2686.